PAPER

Check for updates

Synergistic enhancement of Cu₂Se thermoelectric properties *via* Te and S co-doping: aqueous synthesis and cold-press sintering for power generation†

Vinothkumar Lourdhusamy, [iD] [a] Immanuel Paulraj, [iD] [a] Veera Prabu Kannan [iD] [b] and Chia-Jyi Liu [iD] *[a]

A series of materials, including Cu_2Se, $Cu_2Se_{0.96-x}S_xTe_{0.04}$ ($x = 0.00$, 0.01, 0.02, 0.03), and $Cu_{2-y}Se_{0.94}S_{0.02}Te_{0.04}$ ($y = 0.00$, 0.02, 0.04), were synthesized using aqueous solution processing at room temperature, followed by cold-press sintering under vacuum at 923 K for 6 hours. The samples were extensively characterized by X-ray diffraction and evaluated for their electronic and thermal transport properties. Sulfur doping in $Cu_2Se_{0.96-x}S_xTe_{0.04}$ simultaneously reduces electrical resistivity and thermal conductivity. The composition $Cu_2Se_{0.96-x}S_xTe_{0.04}$ with $x = 0.02$ exhibits the zT of 1.54 at 915 K and the highest average zT of 1.34 between 750 K and 915 K, a 27.62% improvement over $Cu_2Se_{0.96-x}S_xTe_{0.04}$. In the $Cu_{2-y}Se_{0.94}S_{0.02}Te_{0.04}$ series, copper deficiency increases thermal conductivity, leading to a decrease in zT, despite an improved power factor. The sample $Cu_{1.96}Se_{0.94}S_{0.02}Te_{0.04}$ achieves the highest power factor of 10.64 $\mu W\ cm^{-1}\ K^{-2}$, a 5% increase compared to $Cu_2Se_{0.94}S_{0.02}Te_{0.04}$. To assess the practical potential of these materials, a thermoelectric generator (TEG) with eight pairs of p-leg $Cu_2Se_{0.94}S_{0.02}Te_{0.04}$ and n-leg $Cu_{0.7}Ni_{0.3}$ was constructed. The TEG delivers a maximum output voltage of 0.127 V and a peak output power of 21.86 μW at a temperature difference (ΔT) of 120 K. Maximum efficiencies of the p-leg, n-leg, and TEG were 2.0%, 2.25%, and 2.07%, respectively, at $\Delta T = 120$ K and a hot-side temperature of 413 K. These results highlight the potential of the synthesized materials for practical thermoelectric applications.

1. Introduction

Thermoelectric (TE) materials have garnered significant attention for their potential to address environmental pollution and the global energy crisis by converting heat into electricity or *vice versa*, leveraging the Seebeck and Peltier effects.[1] These materials enable solid-state power generation and cooling, offering silent, durable, and emission-free operation. The performance of TE materials is quantified by the dimensionless figure of merit (zT), expressed as

$$zT = \frac{S^2}{\rho(k_e + k_L)}T, \qquad (1)$$

where S is the Seebeck coefficient (thermopower), ρ the electrical resistivity, κ_e the electronic contribution to thermal conductivity,

κ_L the lattice thermal conductivity, and T the absolute temperature.[2] Achieving high zT values necessitates optimizing these interdependent parameters, which present competing demands: a high Seebeck coefficient (indicating strong voltage response to temperature differences), excellent electrical conductivity (minimizing Joule heating losses), and low thermal conductivity (preserving the temperature gradient).[3,4]

Recent research has focused on innovative strategies to decouple these factors, such as nanostructuring, alloying, mobility enhancement, and the development of hybrid organic/ inorganic materials.[5] These approaches hold significant promise for advancing high-performance thermoelectric materials.[6] Enhancing thermoelectric performance typically involves two primary strategies. The first is maximizing the power factor ($S^2\sigma$) through techniques like band convergence engineering, resonant energy levels, carrier filtering, magnetic enhancement, and electron critical behavior. The second is minimizing lattice thermal conductivity using methods such as nanostructuring, entropy engineering, rattling atoms, hierarchical structures, defect engineering, or the exploration of materials with intrinsically low κ_L. Materials exhibiting "phonon-glass electron-crystal" (PGEC) or "phonon-liquid electron-crystal" (PLEC)

[a] Department of Physics, National Changhua University of Education, Changhua 500, Taiwan. E-mail: liucj@cc.ncue.edu.tw

[b] Department of Metallurgical and Materials Engineering, IIT Madras, Chennai 600036, Tamil Nadu, India

† Electronic supplementary information (ESI) available: Details of weighted mobility, EDAX images, XRD, average zT, and thermoelectric properties of n-$Cu_{0.7}Ni_{0.3}$. See DOI: https://doi.org/10.1039/d4ta09047k

This journal is © The Royal Society of Chemistry 2025

J. Mater. Chem. A, 2025, **13**, 6027–6041 | **6027**

behavior are particularly essential for achieving high zT values.[7] The PLEC behavior of Cu_2Se makes it an excellent candidate for thermoelectric applications, especially in high-temperature power generation. With a $zT \geq 1.5$ at $T \approx 1000$ K, Cu_2Se presents a promising alternative to conventional thermoelectric materials such as PbTe, GeTe, and SiGe. Its low lattice thermal conductivity and high electrical conductivity enable high zT values, significantly enhancing thermoelectric efficiency.[8,9]

One of the major challenges in thermoelectric research is the large-scale synthesis of materials that are both cost-effective and energy-efficient. The ability to produce high-performance thermoelectric materials at a lower cost is crucial for making TE technology accessible for widespread applications.[10] Recent studies have highlighted that innovative and cost-effective synthesis methods can substantially improve the performance and applicability of materials like Cu_2Se. For example, Lin et al.[11] demonstrated that Te-doped Cu_2Se synthesized at room temperature achieved a zT value of 1.4 at 920 K. The incorporation of Te not only enhanced material stability but also formed a solid solution with Cu_2Se, improving its thermoelectric properties at lower temperatures. Moreover, various synthesis methods have been explored. Yang et al.[12] reported the fabrication of Te-doped Cu_2Se nanoplates via a solvothermal technique, achieving a zT of 1.8 at 800 K. Similarly, Jia et al.[13] synthesized metastable α-Cu_2Se, obtaining a peak zT of 1.07 at 773 K by controlling the crystal phase. Li et al.[14] utilized wet chemical synthesis to create nanostructured Cu_2Se, reaching a zT of 1.2 at 700 K.

While hydrothermal and solvothermal methods often face challenges in producing pure-phase materials, wet chemical synthesis at room temperature has proven effective. Additionally, studies by Xue et al.[15] and Zhao et al.[16] on sulfur-doped Cu_2Se have demonstrated that these materials can achieve a 30% reduction in thermal conductivity alongside a 30% increase in zT, emphasizing the potential of doping for enhancing thermoelectric performance. Overall, innovations in synthesis methods, particularly those focusing on cost reduction and energy efficiency, are critical for advancing thermoelectric research and expanding the practical applications of materials like Cu_2Se. Wet chemical synthesis of Cu_2Se-based materials presents a promising solution to this challenge, offering a straightforward, low-cost, and scalable approach to creating tailored thermoelectric materials.

The present work investigates the thermoelectric properties of copper selenide-based materials, specifically Cu_2Se and $Cu_{2-y}Se_{0.96-x}S_xTe_{0.04}$, where x and y vary ($x = 0.00, 0.01, 0.02, 0.03$; $y = 0.00, 0.02, 0.04$). These materials were synthesized using aqueous solution methods followed by cold press sintering under vacuum. The study explores the effects of sulfur doping and copper deficiency on thermoelectric performance, focusing on the relationships between doping, carrier concentration, electrical resistivity, and thermal conductivity. The goal is to identify the optimal composition for high thermoelectric efficiency and to provide insights into material design strategies that enhance thermoelectric performance through optimized scattering mechanisms. This research contributes to the development of efficient thermoelectric materials for practical applications.

2. Experimental

2.1 Aqueous synthesis of Cu_2Se and $Cu_{2-y}Se_{0.96-x}S_xTe_{0.04}$ at ambient temperature

Cu_2Se, $Cu_2Se_{0.96-x}S_xTe_{0.04}$ ($x = 0.00, 0.01, 0.02, 0.03$), and $Cu_{2-y}Se_{0.94}S_{0.02}Te_{0.04}$ ($y = 0.00, 0.02, 0.04$) were synthesized using a wet chemical method at room temperature. Initially, $CuCl_2 \cdot 2H_2O$ was dissolved in reverse osmosis (RO) water under continuous stirring at 300 rpm. Selenium (Se), tellurium (Te), and sulfur (S) powders were gradually added to the solution, followed by the controlled addition of $NaBH_4$ as a reducing agent. This addition produced H_2 bubbles and initiated a redox reaction. The resulting precipitates were filtered, washed with RO water, and vacuum-dried at 350 K for 5 hours. The dried powders were cold-pressed into cylindrical pellets and calcined at 923 K for 6 hours under a 20% H_2 and 80% N_2 atmosphere. The calcined materials were subsequently reground, re-pressed, and sintered in a vacuum furnace at 923 K for 6 hours to
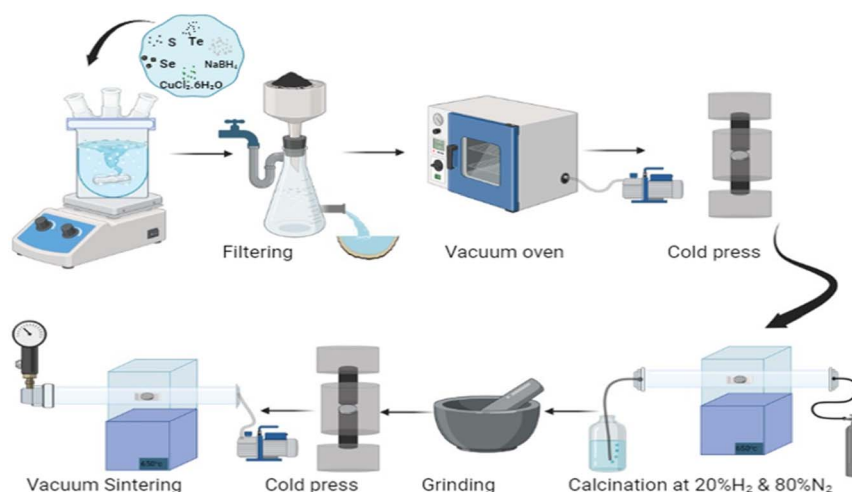

Fig. 1 Schematic diagram of the workflow for the synthesis of Cu_2Se and $Cu_2Se_{0.96-x}S_xTe_{0.04}$ ($x = 0.00, 0.01, 0.02,$ and 0.03).

6028 | J. Mater. Chem. A, 2025, 13, 6027–6041

This journal is © The Royal Society of Chemistry 2025

evaluate their thermoelectric properties. The cylindrical samples were then sliced into rectangular bars for electrical transport measurements. A schematic representation of the synthesis process is shown in Fig. 1.

2.2 Characterization

Phase identification was conducted using a Shimadzu XRD-6000 powder diffractometer with Fe Kα radiation, and the refined lattice parameters were determined using PANalytical X'Pert HighScore Plus software. Microstructural analysis was performed using a Hitachi SU5000 field-emission scanning electron microscope (FESEM). The chemical composition of the materials was semi-quantitatively analyzed *via* energy-dispersive X-ray spectroscopy (EDX) with a Bruker Nano GmbH Flash Detector. The temperature dependence of electrical resistivity and thermopower was measured simultaneously within the range of 325 to 925 K using the Setaram Seebeck Pro system. Hall effect measurements were performed using the van der Pauw method with an applied magnetic field of 0.6 T. Thermal conductivity was determined using a Hot Disk thermal constants analyzer (TPS 2500S), which employs the transient plane source technique to minimize temperature perturbations on the sample. This method utilized a thin sensor element in the shape of a double-spiral nickel (Ni) sensor. Since the Curie temperature of Ni is 627 K, thermal conductivity measurements were not conducted between 575 and 675 K. The uncertainties in the electrical resistivity, Seebeck coefficient, and thermal conductivity measurements were approximately ±10%, ±7%, and ±5%, respectively. The bulk density of the sintered samples was determined using the Archimedes method.

3. Results and discussion

3.1 XRD patterns and FE-SEM micrographs of Cu_2Se and $Cu_2Se_{0.96-x}S_xTe_{0.04}$ (x = 0.00, 0.01, 0.02, and 0.03)

As shown in Fig. 2a, the diffraction patterns of $Cu_2Se_{0.96-x}S_x$-$Te_{0.04}$ align with the characteristic α-Cu_2Se structure (ICDD card #47-1448), confirming that the sintering temperature does not alter the phase composition. These samples exhibit a monoclinic structure with a $C2/c$ space group, consistent with recent reports.[17] Closer examination of Fig. 2b shows a noticeable shift in the (541) diffraction peak toward higher angles with increasing sulfur content. This shift indicates a contraction of the crystal lattice, attributed to the substitution of Se^{2-} ions (radius 1.98 Å) with smaller S^{2-} ions (radius 1.84 Å) on Se^{2-} sites.[18] Additionally, a minor Cu_2O phase was detected as an impurity, with its phase fraction below 2%, as calculated using PANalytical X'Pert HighScore Plus software. Lattice parameters of the samples, listed in Table 1, were determined using PANalytical X'Pert HighScore Plus. Sulfur-doped samples exhibit noticeable shifts in diffraction peaks toward higher angles compared to $Cu_2Se_{0.96}Te_{0.04}$, further confirming the lattice contraction due to sulfur substitution. The porosity (∅) percentage was calculated using

$$\varnothing\% = \left(1 - \frac{\rho_{bulk}}{\rho_{X\text{-}ray}}\right) \times 100, \qquad (2)$$

where ρ_{bulk} is the bulk density and $\rho_{X\text{-}ray}$ the X-ray density of the sample.[19] As shown in Table 1, the bulk density of the sulfur-doped $Cu_2Se_{0.96-x}S_xTe_{0.04}$ exhibits some variation compared to Cu_2Se. Correspondingly, the observed porosity values range from 85.2% to 91.3%.

3.2 FE-SEM

Fig. 3 presents FE-SEM images of the cross-sectional views of Cu_2Se and $Cu_2Se_{0.96-x}S_xTe_{0.04}$ (x = 0.00, 0.01, 0.02, and 0.03), shown in panels (a–e). The FE-SEM images, captured at a magnification of 5 μm, reveal a notable morphological transition from irregular hexagonal plate-like structures to lamellar morphologies across the samples. This morphological transition reflects the influence of sulfur concentrations and their distribution within the Cu_2Se and $Cu_2Se_{0.96-x}S_xTe_{0.04}$ lattice. Among the compositions, $Cu_2Se_{0.96-x}S_xTe_{0.04}$ displays enhanced
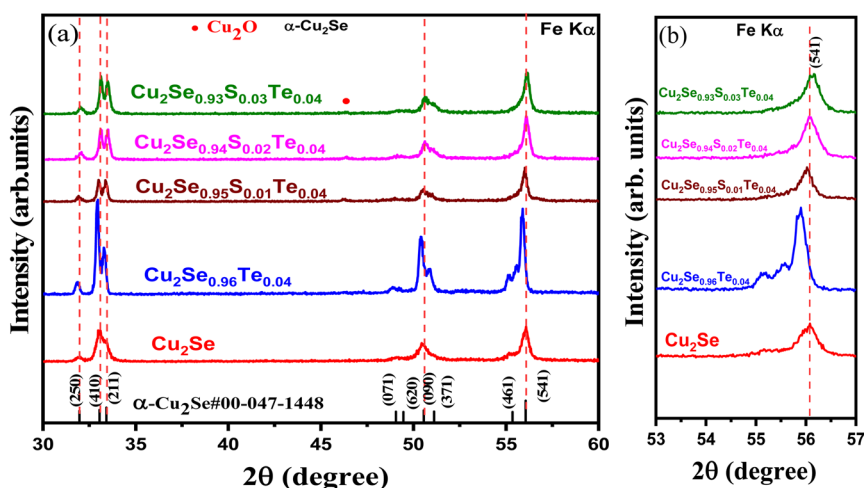

Fig. 2 XRD patterns of Cu_2Se and $Cu_2Se_{0.96-x}S_xTe_{0.04}$ (x = 0.00, 0.01, 0.02, and 0.03): (a) samples sintered at 923 K for 6 h under vacuum, and (b) magnified view for detailed analysis.

Journal of Materials Chemistry A |

Table 1 Lattice parameters, relative density, porosity, carrier concentration, Hall mobility, reduced Fermi energy, effective mass and chemical composition of $Cu_2Se_{0.96-x}S_xTe_{0.04}$ (x = 0.00, 0.01, 0.02, and 0.03)

Crystal system		Monoclinic, (space group $C2/c$)				
		Cu_2Se	$Cu_2Se_{0.96-x}S_xT_{0.04}$	x = 0.01	x = 0.02	x = 0.03
Lattice parameter	a (Å)	7.1484	7.149	7.1356	7.1311	7.1297
	b (Å)	12.314	12.412	12.391	12.388	12.383
	c (Å)	27.558	27.433	27.351	27.348	27.342
	β (°)	94.118	94.443	94.378	94.365	94.36
Relative density (%)	$\frac{\rho_{bulk}}{\rho_{X\text{-}ray}}$ (%)	85.2	88.4	89.2	90	91.3
Porosity (%)	$\varnothing$ (%)	14.8	11.6	10.8	10	8.7
Carrier concentration	n ($\times 10^{20}$ cm^{-3})	5.52	6.58	5.79	5.56	4.78
Hall mobility	μ (cm^2 V^{-1} s^{-1})	12.3	7.8	9.0	11.1	11.9
Reduced Fermi energy (eV)	E_F (eV)	3.425	3.4	3.702	3.8	3.807
Effective mass (m_e)	m^* (m_e)	2.46	2.78	2.36	2.25	2.03
Chemical composition	Cu (at%)	65.03	65.46	66.55	66.23	66.31
	Se (at%)	34.97	33.29	31.71	32.09	31.42
	Te (at%)	0	1.25	1.32	1.15	1.4
	S (at%)	0	0	0.42	0.53	0.87

structural integrity, despite exhibiting a slightly lower density compared to the other samples. This composition emerged as the optimal candidate within the series. EDX analysis confirmed the presence of copper, selenium, tellurium, and sulfur, with the measured chemical compositions closely matching the values provided in Table 1, results are shown in Fig. S1.†
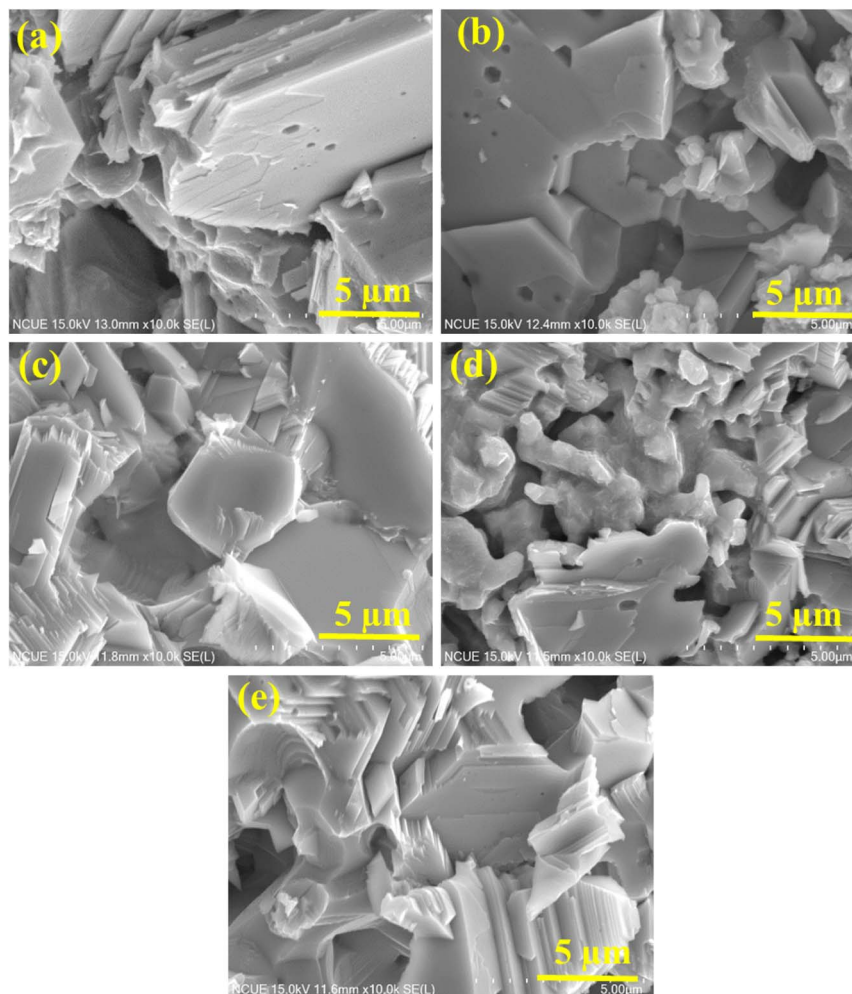
Fig. 3 FE-SEM of (a) Cu_2Se, (b) $Cu_2Se_{0.96}Te_{0.04}$, (c) $Cu_2Se_{0.95}S_{0.01}Te_{0.04}$, (d) $Cu_2Se_{0.94}S_{0.02}Te_{0.04}$, (e) $Cu_2Se_{0.93}S_{0.03}Te_{0.04}$.

3.3 Electronic transport of Cu_2Se and $Cu_2Se_{0.96-x}S_xTe_{0.04}$ (x = 0.00, 0.01, 0.02, and 0.03)

Fig. 4 illustrates the temperature-dependent electronic transport properties of Cu_2Se and $Cu_2Se_{0.96-x}S_xTe_{0.04}$ (x = 0.00, 0.01, 0.02, and 0.03) over the temperature range of 325–925 K. The resistivity increases with temperature, consistent with degenerate semiconductor behavior. Generally, Cu_2Se-based chalcogenides are well-known for their liquid-like behavior and high zT values, it's an electronic–ionic mixed conductor with structural phase transition with temperature. It undergoes phase transition from the low-temperature (LT) monoclinic α-phase to the high-temperature (HT) face-centered cubic (FCC) β-phase ($T_{\alpha \rightarrow \beta}$ ~410 K). In Fig. 4a the undoped Cu_2Se exhibits ρ values of 0.92 mΩ cm at 325 K and 5.21 mΩ cm at 915 K. While Te doping ($Cu_2Se_{0.96}Te_{0.04}$) increases resistivity across the temperature range, likely due to the scattering effect of Te dopants.

Sulfur (S) doping significantly reduces resistivity at all temperatures. Introducing sulfur dopants at concentrations of 0.01, 0.02, and 0.03 reduces ρ across all temperatures. At 325 K, the resistivity values for S-doped samples are 1.20 (x = 0.01),

1.01 (x = 0.02), and 1.10 mΩ cm (x = 0.03), compared to 1.22 mΩ cm for $Cu_2Se_{0.96}Te_{0.04}$. Similarly, at 915 K, S-doped samples show resistivity values of 5.42, 4.64, and 4.34 mΩ cm, respectively, compared to 5.77 mΩ cm for $Cu_2Se_{0.96}Te_{0.04}$. The reduction in resistivity with S doping is attributed to enhanced electrical conductivity due to changes in carrier mobility, as supported by the Hall measurement data (Table 1). Fig. 4b shows the Seebeck coefficient of Cu_2Se and $Cu_2Se_{0.96-x}S_xTe_{0.04}$ (x = 0.00, 0.01, 0.02, and 0.03) across the same temperature range. The Seebeck coefficient decreases with sulfur doping. At 915 K, the Seebeck coefficients are as follows: 223.4 μV K^{-1} for Cu_2Se, 236.1 μV K^{-1} for $Cu_2Se_{0.96}Te_{0.04}$, 218.2 μV K^{-1} for x = 0.01, 217.0 μV K^{-1} for x = 0.02, and 207.75 μV K^{-1} for x = 0.03. Hall measurements at 325 K confirm significant changes in transport properties due to doping. The carrier concentration decreases from 5.52×10^{20} cm^{-3} (Cu_2Se) and 6.58×10^{20} cm^{-3} ($Cu_2Se_{0.96}Te_{0.04}$) to 4.78×10^{20} cm^{-3} ($Cu_2Se_{0.93}S_{0.93}Te_{0.04}$). Despite this decrease in concentration, the slight increase in carrier mobility (from 7.8 cm^2 V^{-1} s^{-1} for $Cu_2Se_{0.96}Te_{0.04}$ to 11.9 cm^2 V^{-1} s^{-1} for $Cu_2Se_{0.93}S_{0.93}Te_{0.04}$) offsets the loss in conductivity, resulting in reduced resistivity.

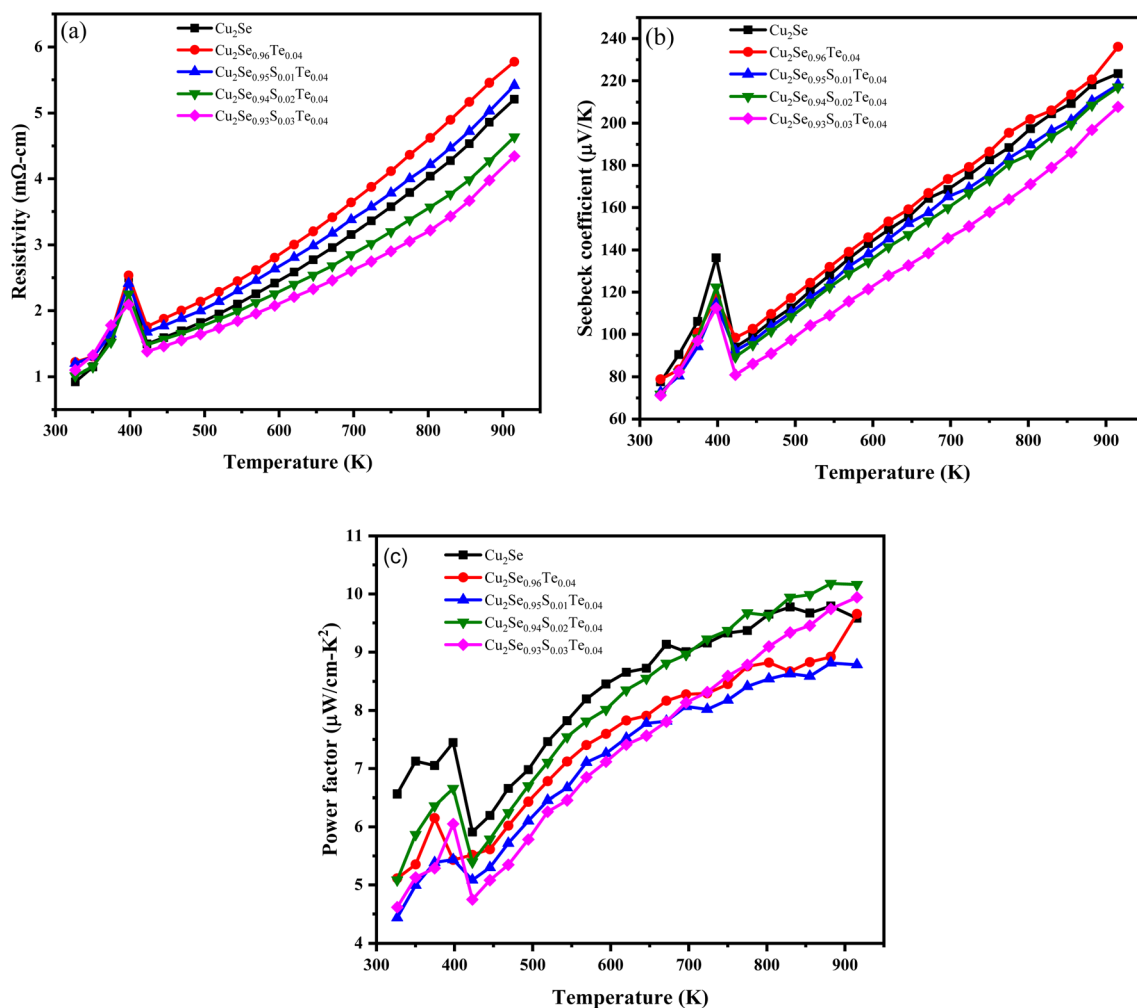**Fig. 4** (a) Electrical resistivity; (b) thermopower; (c) power factor for Cu_2Se and $Cu_2Se_{0.96-x}S_xTe_{0.04}$ (x = 0.00, 0.01, 0.02, and 0.03) sintered at 923 K for 6 h in vacuum.

This journal is © The Royal Society of Chemistry 2025

J. Mater. Chem. A, 2025, **13**, 6027–6041 | **6031**

Positive values in both the Seebeck coefficient and Hall measurements confirm p-type semiconducting behavior, indicating that holes are the dominant charge carriers. Although carrier concentration decreases upon sulfur doping (as shown by Hall measurements), the Seebeck coefficient also decreases. This counterintuitive trend suggests that sulfur doping modifies the band structure or scattering mechanisms, reducing the energy dependence of the carrier transport,[18,20] which offsets the expected increase in the Seebeck coefficient based on the semi-classical Mott–Jones relation,[21–24]

$$S(T) = \frac{8\pi^2 k_B^2}{3eh^2} m^* T \left(\frac{\pi}{3n}\right)^{2/3}, \tag{3}$$

where k_B is the Boltzmann constant, e is the carrier charge, T is temperature, n is the carrier concentration, and m^* is the effective mass of charge carriers.

The changes in mobility are attributed to the small electronegativity difference between sulfur (2.58) and selenium (2.55), which helps minimize perturbation to the local electronic structure, reduce impurity scattering, and hence enhance mobility. While sulfur doping might minimize impurity scattering, it can also introduce new scattering centers (e.g., due to lattice strain or defects). Therefore, the net effect on mobility would depend on the competition between reduced impurity scattering and any additional scattering mechanisms introduced by doping. The Seebeck coefficient depends on carrier concentration and the electronic structure. Sulfur doping might affect the density of states or the band structure, leading to a change in the energy dependence of the transport properties. If the mobility increases but the carrier concentration decreases, it can contribute to balancing electrical transport properties. However, the decrease in resistivity suggests that mobility enhancement might outweigh the reduction in carrier concentration. These factors, along with modifications to the band structure, contribute to the observed decrease in resistivity and the maintenance of moderate Seebeck coefficients, effectively balancing the electrical transport properties for potential thermoelectric applications.[25,26]

Furthermore, we calculate the effective mass and reduced Fermi energy of Cu_2Se and $Cu_2Se_{0.96-x}S_xTe_{0.04}$ using the single-parabolic band (SPB) model.[27] The reduced Fermi energy increases slightly with sulfur doping, rising from 3.425 eV for pristine Cu_2Se to 3.807 eV for the sample with sulfur doping (x = 0.03). This increase suggests that sulfur doping raises the energy required for electrons to reach the conduction band, likely due to modifications in the electronic structure. The upward shift in the Fermi level also indicates a decrease in carrier concentration at higher doping levels, as fewer charge carriers are thermally excited at elevated temperatures. The effective mass decreases from $2.455m_e$ for pristine Cu_2Se to $2.027m_e$ for the sulfur-doped sample with x = 0.03. This reduction in effective mass reflects improved carrier mobility, as carriers with lower effective mass can move more freely through the lattice. These changes suggest that sulfur doping enhances carrier mobility, likely due to alterations in the band structure.

Fig. 4c illustrates the temperature-dependent power factor (PF = σS^2) for Cu_2Se and $Cu_2Se_{0.96-x}S_xTe_{0.04}$ (x = 0, 0.01, 0.02, and 0.03) in the range of 325 to 915 K. At 325 K, pristine Cu_2Se exhibits a PF of approximately 6.56 μW cm^{-1} K^{-2}, while $Cu_2Se_{0.96}Te_{0.04}$ shows a slightly reduced PF of about 5.11 μW cm^{-1} K^{-2}, likely due to Te doping. Upon sulfur doping, the PF values vary, with $Cu_2Se_{0.94}S_{0.02}Te_{0.04}$ achieving the PF value of 5.08 μW cm^{-1} K^{-2} at 325 K. As temperature increases, all samples exhibit significant enhancement in PF. At 915 K, pristine Cu_2Se reaches approximately 9.58 μW cm^{-1} K^{-2}, while $Cu_2Se_{0.96}Te_{0.04}$ achieves 9.65 μW cm^{-1} K^{-2}. Among the sulfur-doped samples, $Cu_2Se_{0.94}S_{0.02}Te_{0.04}$ demonstrates superior thermoelectric performance, reaching the highest PF of 10.16 μW cm^{-1} K^{-2}. These trends underscore the critical role of sulfur doping in optimizing the power factor through its influence on carrier mobility and scattering mechanisms, as well as its impact on the density of states or band structure, balancing electrical conductivity and Seebeck coefficient.[26]

3.4 Thermal transport of zT and zT_{avg} of Cu_2Se and $Cu_2Se_{0.96-x}S_xTe_{0.04}$ (x = 0.00, 0.01, 0.02, and 0.03)

Fig. 5 illustrates the temperature dependence of thermal transport of Cu_2Se and $Cu_2Se_{0.96-x}S_xTe_{0.04}$ (x = 0, 0.01, 0.02, and 0.03) over the temperature range of 325–725 K. Thermal conductivity (κ) was measured using a Hot Disc 2500S setup equipped with a double-spiral Ni sensor. Measurements were omitted between 575 and 675 K due to the Curie temperature of nickel (627 K), which limits the functionality of the sensor.

3.4.1 Total thermal conductivity κ. As shown in Fig. 5a, the total thermal conductivity for all samples remains below 1.23 W m^{-1} K^{-1}, consistent with low thermal conductivity typical of liquid-like behavior. Sulfur doping further reduces κ compared to undoped $Cu_2Se_{0.96}Te_{0.04}$. This reduction arises from sulfur incorporation on selenium sites, which introduces point defects and enhances phonon scattering. Additionally, sulfur doping decreases the carrier concentration,[16] as reported in previous studies, contributing to reduced κ.[28] At 325 K, pristine Cu_2Se exhibits a κ of 1.23 W m^{-1} K^{-1}, slightly higher than $Cu_2Se_{0.96}Te_{0.04}$ at 1.22 W m^{-1} K^{-1}. With increasing temperature, κ decreases for all samples due to phonon-dominated heat transport.[29,30] At 725 K, κ drops to 0.69 W m^{-1} K^{-1} for Cu_2Se and 0.68 W m^{-1} K^{-1} for $Cu_2Se_{0.96}Te_{0.04}$. For sulfur-doped samples, the κ reduction is more pronounced. The sample with x = 0.01 shows κ = 1.183 W m^{-1} K^{-1} at 325 K, decreasing to 0.652 W m^{-1} K^{-1} at 725 K. Similarly, the x = 0.02 sample shows κ = 1.036 W m^{-1} K^{-1} at 325 K and decreases to 0.652 W m^{-1} K^{-1} at 725 K. The x = 0.03 sample has the lowest values, starting at 1.011 W m^{-1} K^{-1} at 325 K and reducing to 0.613 W m^{-1} K^{-1} at 725 K. These results demonstrate the effectiveness of sulfur doping in reducing κ by altering phononic transport properties.[29,30]

3.4.2 Electronic thermal conductivity (κ_e). Fig. 5b shows the electronic thermal conductivity (κ_e), which is calculated using the Wiedemann–Franz law assuming that the relaxation times for both electronic and thermal processes are identical: $\kappa_e = \sigma L T$, where σ is the electrical conductivity, L is the Lorenz number, and T is the temperature. The Lorenz number was
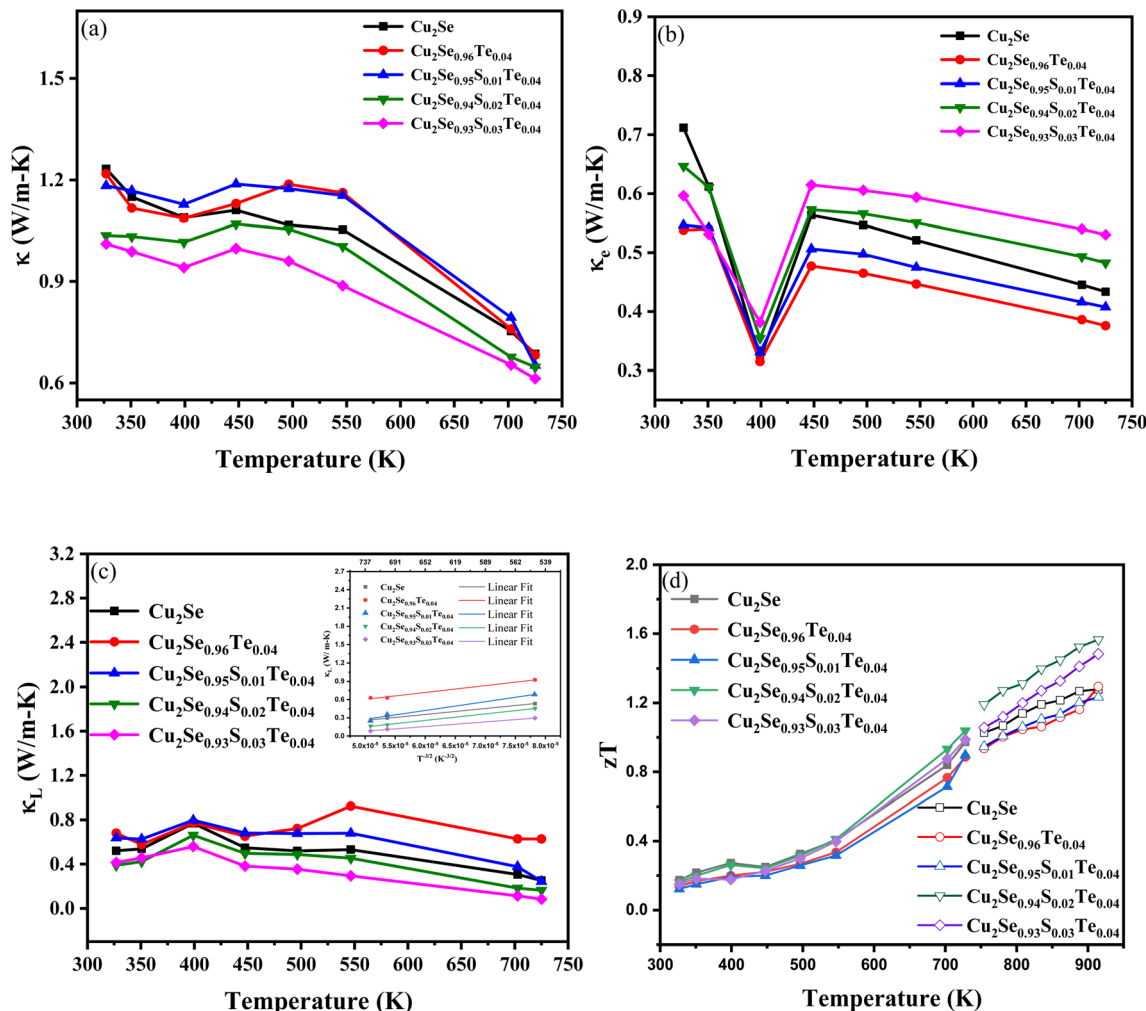
6032 | J. Mater. Chem. A, 2025, **13**, 6027–6041

This journal is © The Royal Society of Chemistry 2025

Fig. 5 (a) Total thermal conductivity (κ); (b) electronic thermal conductivity (κ_e); (c) lattice thermal conductivity (κ_L) and inset the fig $\kappa_L \sim T^{-3/2}$; (d) zT for Cu_2Se and $Cu_2Se_{0.96-x}S_xTe_{0.04}$ (x = 0, 0.01, 0.02, and 0.03) sintered at 923 K for 6 h in vacuum.

determined based on the reduced Fermi energy (η) derived from the Seebeck coefficient, assuming dominant acoustic phonon scattering. The expressions as outlined in eqn (4)–(6),[31]

$$L = \left(\frac{k_B}{e}\right)^2 \frac{(3F_0(\eta)F_2(\eta) - 4F_1^2(\eta))}{F_1^2(\eta)}, \quad (4)$$

$$F_n(\eta) = \int_0^\infty \frac{x^n}{1 + \exp(x - \eta)} dx, \quad (5)$$

$$S = \pm \frac{k_B}{e} \left(\frac{2F_1(\eta)}{F_0(\eta)} - \eta\right), \quad (6)$$

where k_B is the Boltzmann constant ($1.38064852 \times 10^{-23}$ J K^{-1}), e the elementary charge (1.6×10^{-19} C), $\eta = \frac{E_F}{k_B T}$ the reduced Fermi energy, E_F the Fermi energy, and $F_n(\eta)$ the Fermi integral. We calculate the Lorenz number using the SPBcal algorithm.[27] At 325 K, Cu_2Se exhibits higher κ_e than those of $Cu_2Se_{0.96}Te_{0.04}$ and sulfur-doped samples, highlighting the contribution of electronic heat transport. With increasing temperature, κ_e

decreases in all samples, indicating the growing influence of phonon scattering.

3.4.3 Lattice thermal conductivity (κ_L). Fig. 5c depicts κ_L, obtained by subtracting κ_e from the total κ. All samples exhibit low κ_L values ranging from 0.68 to 0.42 W m^{-1} K^{-1}. Between 325 K and 500 K, κ_L decreases non-linearly and follows a $\kappa_L \sim T^{-3/2}$ trend beyond 500 K, as shown in the inset of Fig. 5c.[32] This trend confirms acoustic phonon scattering as the dominant mechanism governing lattice thermal conductivity. The observation that the lattice thermal conductivities of two Te-doped samples ($Cu_2Se_{0.96}Te_{0.04}$ and $Cu_2Se_{0.95}S_{0.01}Te_{0.04}$) are higher than that of pristine Cu_2Se, as shown in Fig. 5c, can be attributed to the complex interplay of doping effects on the superionic lattice structure and phonon scattering mechanisms. While doping is often associated with a reduction in thermal conductivity due to enhanced phonon scattering, the higher lattice thermal conductivity in these two samples indicates competing mechanisms at play. It might arise from a combination of reduced anharmonicity, lattice stiffening, and changes in phonon transport dynamics due to Te doping. The stabilization of the

This journal is © The Royal Society of Chemistry 2025

J. Mater. Chem. A, 2025, **13**, 6027–6041 | **6033**

lattice by Te atoms decreases Cu ionic mobility, reducing phonon scattering and enhancing thermal conductivity.

3.4.4 Dimensionless figure of merit (zT). Fig. 5d shows the dimensionless figure of merit (zT) for Cu_2Se and $Cu_2Se_{0.96-x}$-$S_xTe_{0.04}$ ($x = 0.00$, 0.01, 0.02, and 0.03) between 325 and 915 K. The zT values of all samples increase with rising temperature, which reflects improvements in thermoelectric performance. The sulfur doping to selenium-based samples enhances the zT across the entire temperature range. This improvement is attributed to factors such as optimal hole concentrations, reduced carrier and lattice thermal conductivities, and sustained high power factors (PFs). The maximum zT value of 1.56 for $Cu_2Se_{0.94}S_{0.02}Te_{0.04}$ is achieved at 915 K, representing a 22.83% increase compared to Cu_2Se. The open symbols indicate the calculated zT values at the maximum temperature ($T \geq T_{\kappa,\max}$), where $T_{\kappa,\max}$, is the maximum temperature in the thermal conductivity measurements. Notably, the total thermal conductivity decreases with increasing temperature, emphasizing the importance of optimizing sulfur concentration to enhance thermoelectric performance, as demonstrated by the favorable zT values for the $x = 0.02$ sample.

A high-performance thermoelectric material not only requires a high zT value but also a high average zT (zT_{avg}) across the operating temperature range. The average figure of merit, zT_{avg}, is defined as

$$zT_{\mathrm{avg}} = \frac{1}{T_H - T_c} \int_{T_c}^{T_H} zT \mathrm{d}T, \tag{7}$$

where T_H and T_C are the hot and cold side temperature, Fig. 6 illustrates the calculation of zT_{avg} as the integral of zT over the specified temperature range, as per eqn (7). In this study, the zT_{avg} values of Cu_2Se and $Cu_2Se_{0.96-x}S_xTe_{0.04}$ ($x = 0.00$, 0.01, 0.02, and 0.03) were analyzed over the temperature range of 750 to 915 K. With sulfur doping, the zT_{avg} values increase significantly, from 1.14 for undoped Cu_2Se to 1.05, 1.06, 1.34, and 1.22 for $x = 0.00$, 0.01, 0.02, and 0.03, respectively. Notably, the sample with x

$= 0.02$ exhibits the highest zT_{avg} of 1.34, representing a 27.62% improvement compared to the undoped $x = 0.00$ sample. In addition, the $x = 0.02$ sample demonstrates the maximum average zT values of 0.47 and 0.75 over the temperature ranges of 325–725 K and 325–915 K, respectively. These enhancements are attributed to sulfur doping, which optimizes hole concentration, reduces lattice thermal conductivity, and improves the power factor. To further contextualize the results, Table 2 compares the fabrication methods, power factors, and zT values at high temperatures between this study and recent literature. The findings underscore the efficacy of sulfur as a dopant for improving the thermoelectric performance of Cu_2Se.

In conclusion, sulfur doping significantly enhances the thermoelectric properties of Cu_2Se. Among the samples, the $x = 0.02$ composition achieves the highest zT and zT_{avg}, highlighting the effectiveness of sulfur doping in optimizing thermoelectric materials for high-performance applications.

3.5 XRD patterns and FE-SEM micrographs of $Cu_{2-y}Se_{0.94}S_{0.02}Te_{0.04}$ ($y = 0.00$, 0.02, and 0.04)

Previous studies have reported that copper deficiency can decrease electrical resistivity by increasing the hole carrier concentration.[32] In this study, we examined the effects of copper deficiency on the structural and physical properties of Cu_{2-y}-$Se_{0.94}S_{0.02}Te_{0.04}$ with varying deficiency levels ($y = 0.00$, 0.02, and 0.04). Fig. S2a† presents the XRD patterns of the samples sintered at 923 K, where all diffraction peaks correspond to the α-Cu_2Se phase (ICDD card no. 47-1448). This confirms that the phase remains unchanged with increasing copper deficiency. However, as shown in Fig. S2b,† a shift in the (620) and (541) diffraction peaks toward higher angles is observed with increasing copper deficiency, indicating subtle structural changes. The lattice parameters, density, and porosity of the samples vary with the degree of copper deficiency. For the sample with $y = 0.02$ ($Cu_{1.98}Se_{0.94}S_{0.02}Te_{0.04}$), $a = 7.1295$ Å, $b = 12.411$ Å, and $c = 27.359$ Å, with a β angle of 94.42°. This sample exhibits a relative density of 89% and a porosity of 11%. The elemental composition is 66.02% Cu, 32.21% Se, 1.13% Te, and 0.46% S. In comparison, the sample with $y = 0.04$ ($Cu_{1.96}Se_{0.94}S_{0.02}Te_{0.04}$) shows slightly reduced lattice constants ($a = 7.1289$ Å, $b = 12.401$ Å, $c = 27.354$ Å) and a marginally altered β angle of 94.46°. This sample exhibits a relative density of 88.35% and a porosity of 11.65%, with an elemental composition of 66.09% Cu, 32.25% Se, 1.24% Te, and 0.42% S. These results reveal that increasing copper deficiency leads to slight reductions in lattice constants, a decrease in relative density, and an increase in porosity. These structural changes provide valuable insights into the relationship between copper deficiency and the physical properties of $Cu_{2-y}Se_{0.94}S_{0.02}Te_{0.04}$, which is critical for optimizing its thermoelectric performance. As seen in Fig. S3(a–f),† the FE-SEM images and EDS spectra show the morphology and elemental composition of $Cu_{2-y}Se_{0.94}S_{0.02}Te_{0.04}$ with varying copper deficiency ($y = 0.00$, $y = 0.02$, and $y = 0.04$). The FE-SEM images in Fig. S3a, c, and e† reveal a stacked plate-like nanostructure across all compositions. Despite the visual similarities in morphology, the elemental analyses *via* EDS in Fig. S3b, d, and f† confirm the
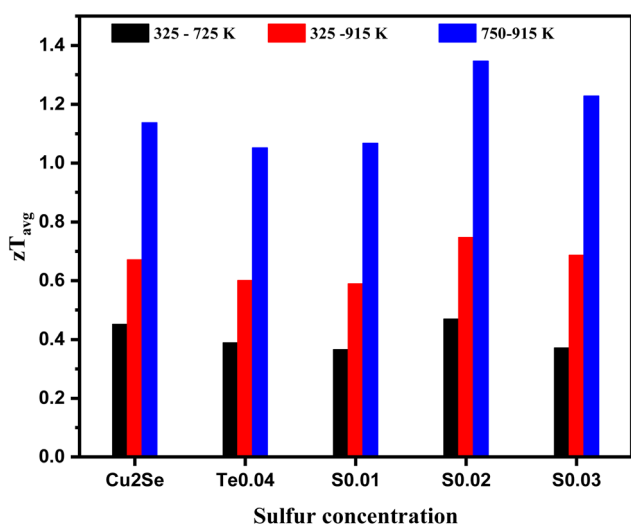

Fig. 6 Average zT (zT_{avg}) for Cu_2Se and $Cu_2Se_{0.96-x}S_xTe_{0.04}$ ($x = 0.00$, 0.01, 0.02, and 0.03) sintered at 923 K for 6 h in vacuum.

6034 | *J. Mater. Chem. A*, 2025, **13**, 6027–6041

This journal is © The Royal Society of Chemistry 2025

Table 2 Comparison of synthetic method, power factor, and zT values among Cu_2Se-based materials

Material	Synthesis method + sintering	Power factor ($\mu W\ cm^{-1}\ K^{-2}$)	zT	T (K)	Ref.
Cu_2Se	Ball milling + 3D printing + sintering at 873 K	8.5	1.21	1000	33
Cu_2Se	Sputtering + 573 K annealing	11.1	0.42	550	34
Br doped Cu_2Se	Evacuated quartz tube melting + hot press sintering 873 K	6.1	0.51	560	35
Cu_2Se	Pyrolytic boron nitride crucible enclosed in a fused silica tube at 1423 K for 12 h in vacuum melting + SPS@710 K	11.2	1.5	1000	36
$(Cu_2Se)_{0.97}(SnSe)_{0.03}$	Evacuated quartz tube melting + ball milling SPS @ 923 K	12	1.4	823	37
$Li_{0.09}Cu_{1.9}Se$	Evacuation melting + ball mill + hot-press @ 973 K	10.4	1.4	1000	38
$Cu_2Se/0.75\ wt\%\ CNT$	Ball milling + SPS @ 753 K	9	2.4	1000	7
$Cu_2Se_{0.96}Te_{0.04}$	Aqueous solution synthesis at RT + cold-press sintering in vacuum @ 923 K	9.9	1.4	920	11
$Cu_2Se_{0.96}Te_{0.02}I_{0.02}/Cu_2O$	Aqueous solution synthesis at RT + cold-press sintering in vacuum @ 923 K	9.1	0.47	550	17
$Cu_2Se_{0.94}S_{0.02}Te_{0.04}$		10.16	1.56	915	This work

systematic variation in copper content with increasing deficiency levels. The EDS spectra demonstrate the presence of Cu, Se, Te, and S elements in proportions consistent with the nominal compositions, further validating the accuracy of the doping process.

3.6 Electronic transport of $Cu_{2-y}Se_{0.94}S_{0.02}Te_{0.04}$ ($y = 0.00$, 0.02, and 0.04)

As shown in Fig. 7a, the electrical resistivity of $Cu_{2-y}Se_{0.02}Te_{0.04}$ ($y = 0.00$, 0.02, and 0.04) decreases with increasing copper deficiency below 645 K. For instance, introducing

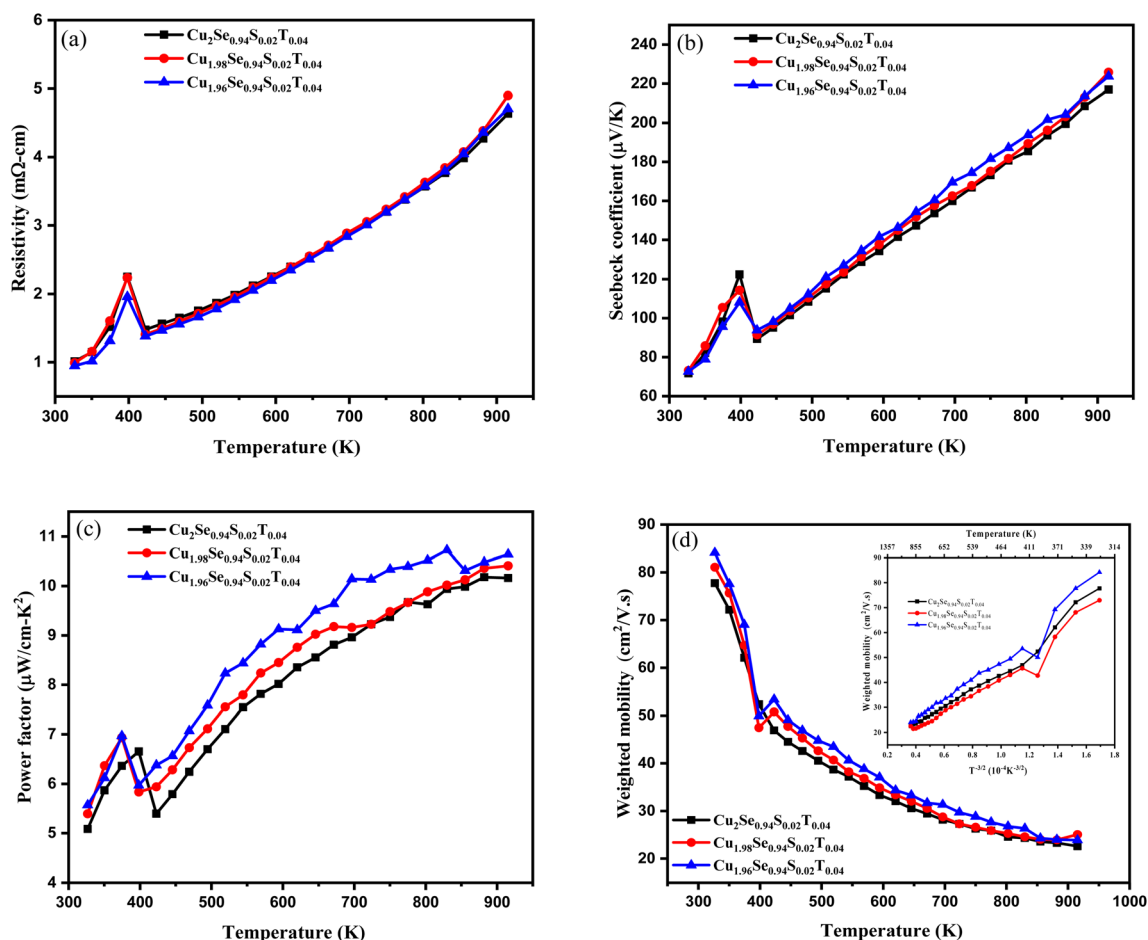**Fig. 7** (a) Electrical resistivity; (b) thermopower; (c) power factor; (d) weighted mobility and inset weighted mobility vs. $T^{-3/2}$ for $Cu_{2-y}Se_{0.94}S_{0.02}Te_{0.04}$ ($y = 0.00$, 0.02, and 0.04) sintered at 923 K for 6 h in vacuum.

This journal is © The Royal Society of Chemistry 2025

J. Mater. Chem. A, 2025, **13**, 6027–6041 | **6035**

copper vacancies reduces the resistivity from 1.10 mΩ cm for $Cu_{2-y}Se_{0.94}S_{0.02}Te_{0.04}$ ($y = 0.00$) to 0.95 mΩ cm for $y = 0.04$ at 325 K, due to an increase in carrier concentration from the added vacancies. However, at higher temperatures, the resistivity of the copper-deficient sample exceeds that of the sample without copper vacancies ($y = 0.00$). This seemingly anomalous behavior can be explained by the interplay between carrier concentration and carrier scattering mechanisms at elevated temperatures. While copper vacancies increase the carrier concentration, leading to lower resistivity at low temperatures, the higher carrier density also intensifies electron–electron scattering at elevated temperatures. Additionally, phonon scattering becomes more pronounced as temperature rises, further contributing to the resistivity increase. The combined effect of these scattering mechanisms at high temperatures outweighs the resistivity-lowering influence of increased carrier concentration. As a result, $y = 0.02$ sample above 645 K and the $y = 0.04$ sample above 800 K both exhibit higher resistivity compared to the $y = 0.00$ sample at elevated temperatures. The carrier concentration of $Cu_{2-y}Se_{0.94}S_{0.02}Te_{0.04}$ at 325 K increases with copper deficiency, rising from 5.56×10^{20} cm^{-3} for $y = 0.00$ to 6.65×10^{20} cm^{-3} for $y = 0.02$

and 7.57×10^{20} cm^{-3} for $y = 0.04$. This increase is primarily attributed to the formation of Cu vacancies within the crystal lattice, which act as acceptor-like defects, introducing holes as charge carriers through impurity states within the bandgap. However, charge carrier mobility decreases with increasing copper deficiency, dropping from 11.1 cm^2 V^{-1} s^{-1} for $y = 0.00$ to 9.5 cm^2 V^{-1} s^{-1} for $y = 0.02$ and 8.7 cm^2 V^{-1} s^{-1} for $y = 0.04$. This reduction is mainly due to the higher carrier concentration and the role of Cu vacancies as scattering centers, which impede charge carrier transport. These findings underscore the dual effects of Cu deficiency on modulating carrier concentration and mobility, shaping the overall transport properties of the material.

The Seebeck coefficient of $Cu_{2-y}Se_{0.94}S_{0.02}Te_{0.04}$ exhibits distinct trends across different phases and temperatures. Introducing Cu deficiency ($y = 0.02$ and $y = 0.04$) slightly enhances the Seebeck coefficient compared to $Cu_2Se_{0.94}S_{0.02}Te_{0.04}$. In the α-phase (325–400 K), the Seebeck coefficient ranges from 71.8 to 114.3 μV K^{-1}, showing strong temperature dependence. In the β-phase (425–915 K), it spans a wider range, from 89.3 to 225.8 μV K^{-1}, reflecting substantial variability with temperature changes, as shown in Fig. 7b. The power factor (PF)
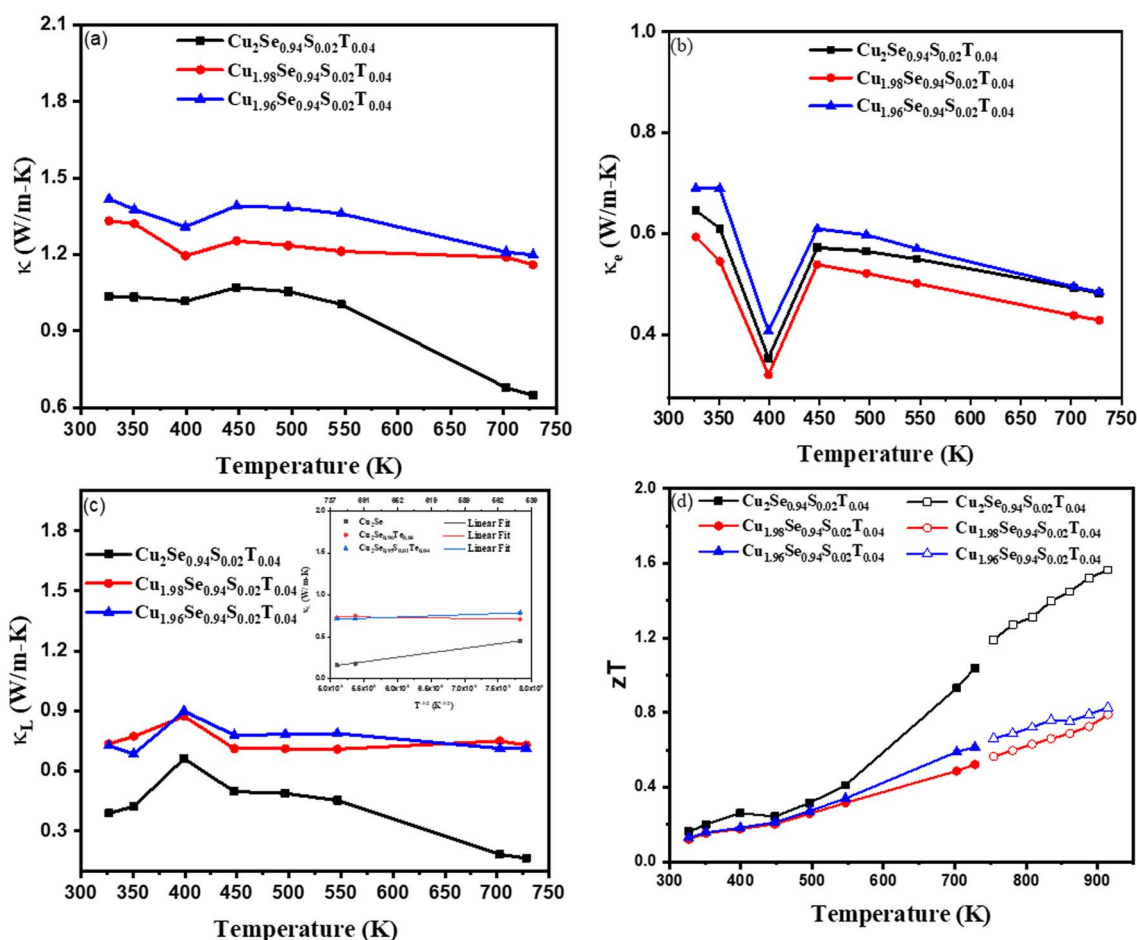

Fig. 8 (a) Total thermal conductivity (κ); (b) electronic thermal conductivity (κ_e); (c) lattice thermal conductivity (κ_L) and inset with $\kappa_L \sim T^{-3/2}$; (d) zT for $Cu_{2-y}Se_{0.94}S_{0.02}Te_{0.04}$ ($y = 0.00$, 0.02, and 0.04) sintered at 923 K for 6 h in vacuum.

6036 | J. Mater. Chem. A, 2025, 13, 6027–6041

This journal is © The Royal Society of Chemistry 2025

of $Cu_{2-y}Se_{0.94}S_{0.02}Te_{0.04}$, presented in Fig. 7c, increases with temperature for all samples, consistent with literature on Cu-deficient materials. The power factors at 325 K (915 K) and are as follows: 5.08 (10.16), 4.85 (9.83), and 5.57 (10.63) $\mu W\ cm^{-1}\ K^{-2}$ for $y = 0.00$, 0.02, and 0.04, respectively. Notably, the $y = 0.04$ sample achieves a 9.48% increase in PF compared to $Cu_2Se_{0.94}S_{0.02}Te_{0.04}$, underscoring the beneficial effects of Cu vacancies on thermoelectric performance. Fig. 7d shows the temperature dependence of the weighted mobility (μ_W) for $Cu_{2-y}Se_{0.94}S_{0.02}Te_{0.04}$ with $y = 0.02$ and $y = 0.04$. The mobility decreases with increasing temperature.[39,40] The μ_W values range from 77.75 to 84.21 $cm^2\ V^{-1}$. The inset plot further confirms that charge carriers are primarily scattered by acoustic phonons, as evidenced by the μ_W following a $T^{-3/2}$ dependence as shown in Fig. 7d. The weighted mobility of the Cu_2Se and $Cu_2Se_{0.96-x}S_xTe_{0.04}$ (where $x = 0.00$, 0.01, 0.02, and 0.03) was determined using eqn (S1).†[41]

3.7 Thermal transport, zT and zT_{avg} of $Cu_{2-y}Se_{0.94}S_{0.02}Te_{0.04}$ ($y = 0.00$, 0.02, and 0.04)

Fig. 8a illustrates the thermal transport properties of $Cu_{2-y}Se_{0.94}S_{0.02}Te_{0.04}$ with $y = 0.00$, 0.02, and 0.04. For samples with $y = 0.02$ and $y = 0.04$, the thermal conductivity decreases with increasing temperature, following typical behavior. However, upon introducing copper deficiency, the thermal conductivity increases. Across the entire temperature range, the sample with $y = 0.00$ consistently exhibits the lowest thermal conductivity, ranging from 1.036 $W\ m^{-1}\ K^{-1}$ at lower temperatures to 0.647 $W\ m^{-1}\ K^{-1}$ at higher temperatures. In contrast, the $y = 0.02$ sample has thermal conductivity values ranging from 1.33 to 1.159 $W\ m^{-1}\ K^{-1}$, while the $y = 0.04$ sample shows the highest values, spanning 1.417 to 1.198 $W\ m^{-1}\ K^{-1}$. Fig. 8b presents the calculated electronic thermal conductivity (κ_e) for $Cu_{2-y}Se_{0.94}S_{0.02}Te_{0.04}$ with $y = 0.00$, 0.02, and 0.04, which decreases monotonically with increasing temperature for the β-phase due to the reduction in electrical conductivity. Fig. 8c shows the lattice thermal conductivity (κ_L), which generally decreases with increasing temperature for the β-phase due to enhanced phonon scattering at higher temperatures. However, for the $y = 0.02$ sample, an anomalous increase in κ_L is observed at higher temperatures. Fig. 8d shows the calculated dimensionless thermoelectric figure of merit (zT) of $Cu_{2-y}Se_{0.94}S_{0.02}Te_{0.04}$. Among all samples, the $y = 0.00$ sample has the highest zT across the temperature range, primarily due to its lower thermal conductivity. In contrast, the copper-deficient samples ($y = 0.02$ and $y = 0.04$) exhibit reduced zT values, attributed to higher thermal conductivity resulting from increased carrier concentrations. The $y = 0.00$ sample has the maximum zT of 1.56 at 915 K, as indicated by the open symbols. Fig. S4† displays the average zT (zT_{avg}) values for $Cu_{2-y}Se_{0.94}S_{0.02}Te_{0.04}$ ($y = 0.00$, 0.02, and 0.04) in different temperature ranges (325–725 K, 325–915 K, and 750–915 K). The $y = 0.00$ sample achieves the highest zT_{avg} of 1.34 within the 750–915 K range, while the copper-deficient samples show reduced zT_{avg} values of 0.64 and 0.72 for $y = 0.02$ and $y = 0.04$, respectively.

4. Thermoelectric properties of n-$Cu_{0.7}Ni_{0.3}$

Fig. S5† presents the XRD patterns and the temperature-dependent electronic and thermal transport of $Cu_{0.7}Ni_{0.3}$, synthesized via hydrothermal methods followed by evacuated-and-encapsulated sintering.[22] In Fig. S5a,† the XRD pattern obtained using Fe Kα radiation reveals diffraction peaks corresponding to a face-centered cubic (FCC) lattice with space group $Fm\bar{3}m$ (# 225), consistent with ICDD card number 47-1406. As seen in Fig. S5(b–f),† in the temperature range of 325–550 K, the electrical conductivity (σ) exhibits weak temperature dependence, characteristic of disordered transition metal alloys. At 325 K and 500 K, σ is measured as 16.04 and 15.18 mΩ cm, respectively. The negative Seebeck coefficient confirms the n-type behavior of $Cu_{0.7}Ni_{0.3}$, changing in magnitude from -33.68 $\mu V\ K^{-1}$ at 325 K to -48.75 $\mu V\ K^{-1}$ at 500 K. The power factor ($S^2\sigma$) reaches values of 18.14 and 36.18 $\mu W\ cm^{-1}\ K^{-2}$ at 325 and 500 K respectively. The total thermal conductivity (κ) rises from 3.64 $W\ m^{-1}\ K^{-1}$ at 325 K to 4.50 $W\ m^{-1}\ K^{-1}$ at 550 K. Consequently, the zT value of $Cu_{0.7}Ni_{0.3}$ increases from 0.16 at 325 K to 0.44 at 550 K, demonstrating enhanced thermoelectric performance at elevated temperatures.

5. Performance of a thermoelectric generator (TEG) comprising 8 pairs of p-leg

5.1 $Cu_2Se_{0.94}S_{0.02}Te_{0.04}$ and n-leg $Cu_{0.7}Ni_{0.3}$

A thermoelectric generator was fabricated using 8 pairs of p-leg $Cu_2Se_{0.94}S_{0.02}Te_{0.04}$ and n-leg $Cu_{0.7}Ni_{0.3}$. The schematic of the device is shown in Fig. 9a. Fig. 9b presents the current–voltage ($I–V$) characteristics at various temperature differences (ΔT), showing linear behavior where the output voltage decreases with increasing current. In Fig. 9c, the output voltage is plotted as a function of ΔT ($\Delta T = T_H - T_C$, where T_H and T_C represent the hot and cold side temperatures of the device). The output voltage increases with ΔT, peaking at 0.127 V for $\Delta T = 120$ K (inset: photographs of the fabricated TEG and the measurement setup). Fig. 9d shows the relationship between load resistance and output voltage at different ΔT values ranging from 7 K to 120 K. The maximum voltage (V_{max}) increases with ΔT, rising from 3.8 mV at $\Delta T = 7$ K to 9.7, 14.7, 19.9, 31.9, 52.6, 70.5, and 127 mV for $\Delta T = 20$, 30, 40, 60, 80, 100, and 120 K, respectively. Fig. 9e illustrates the electrical output power as a function of output current at various ΔT. The maximum output power (P_{max}) of the TEG was calculated using eqn (8)

$$P_{max} = \frac{E^2 R_{load}}{(R_{internal} + R_{load})^2}, \qquad (8)$$

where E is the output voltage (mV), R_{load} is the load resistance (Ω), and $R_{internal}$ is the internal resistance of the TEG (Ω). The P–I curves show that maximum power occurs when $R_{internal}$ matches R_{load}. The output power increases from 0.05 μW at $\Delta T = 7$ K to 0.30, 0.64, 1.09, 2.46, 5.39, 13.58, and 21.86 μW for $\Delta T = 20$, 30,
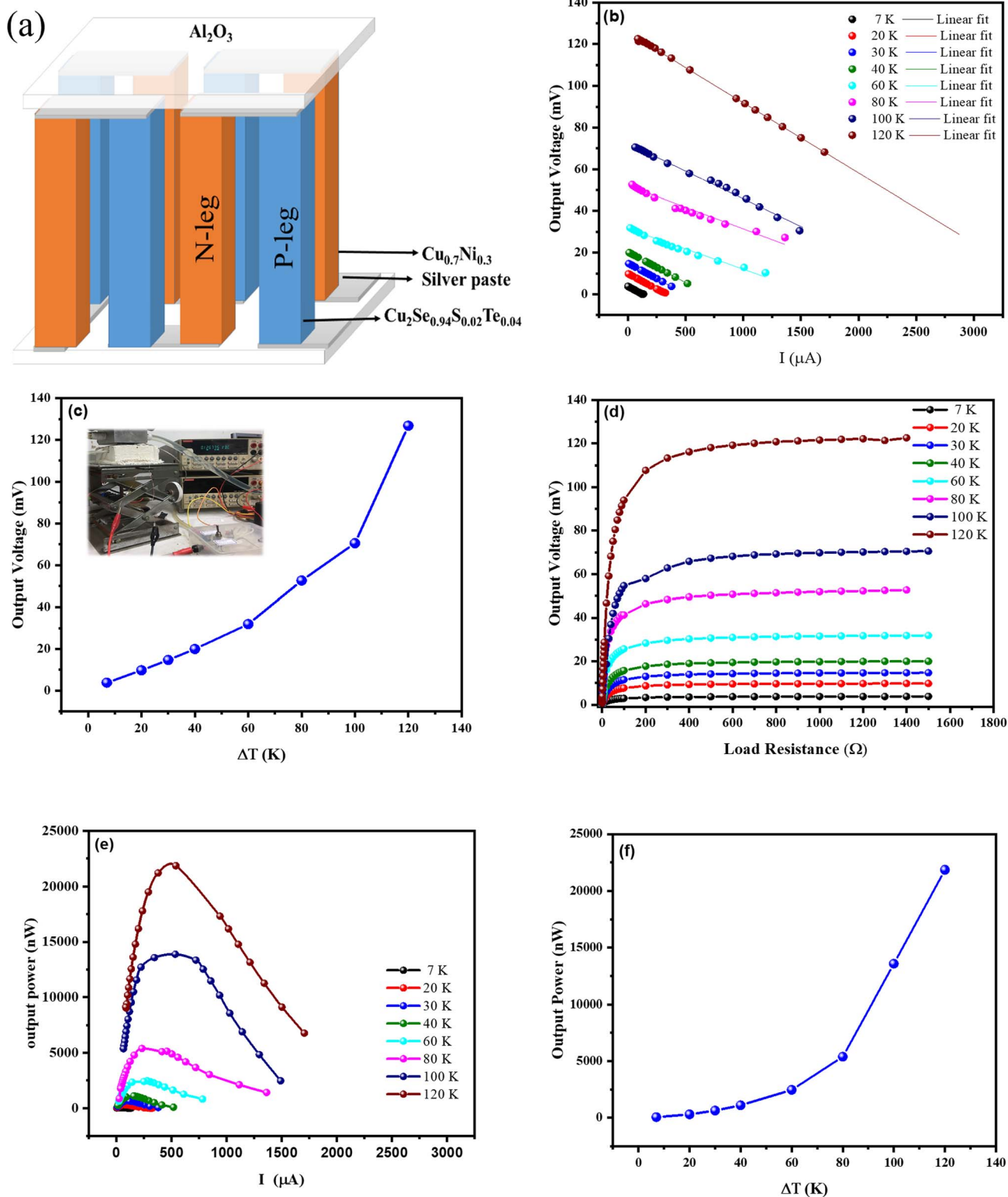
This journal is © The Royal Society of Chemistry 2025

J. Mater. Chem. A, 2025, **13**, 6027–6041 | **6037**

Fig. 9 A thermoelectric generator comprising 8 pairs of p-leg ($Cu_2Se_{0.94}S_{0.02}Te_{0.04}$) and n-leg ($Cu_{0.7}Ni_{0.3}$). (a) Schematic of the fabricated device; (b) output voltage *versus* output current at various temperature differences (ΔT); (c) output voltage as a function of ΔT (inset: photographs of the fabricated TEG and measurement setup); (d) voltage *versus* load resistance (R_{load}) at various ΔT; (e) output power *versus* output current at various ΔT; (f) maximum output power (P_{max}) as a function of ΔT.

6038 | *J. Mater. Chem. A*, 2025, **13**, 6027–6041

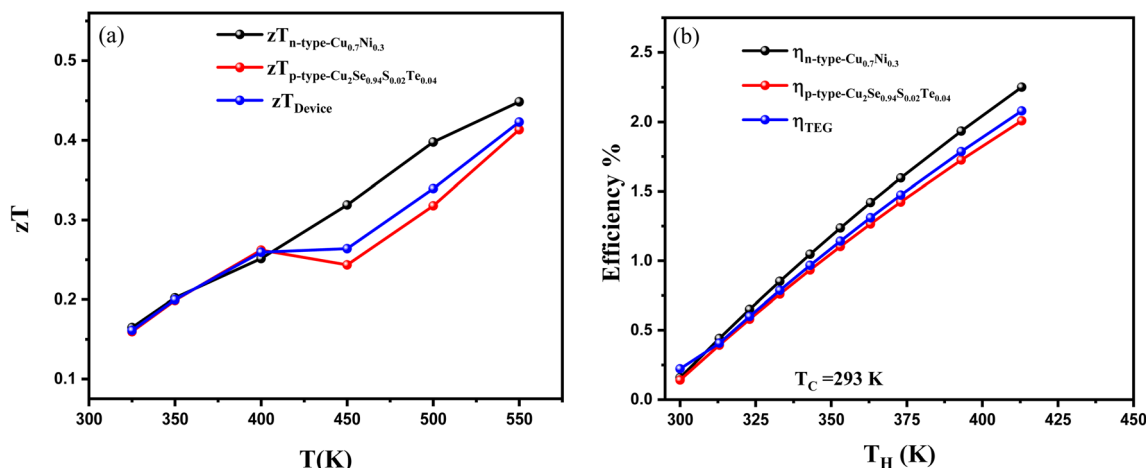This journal is © The Royal Society of Chemistry 2025

Fig. 10 (a) Temperature dependence of zT for p-leg, n-leg, and the fabricated TEG; (b) temperature dependence of efficiency for p-leg, n-leg, and the fabricated TEG at $\Delta T = 120$ K.

Table 3 Comparison of the TEG fabricated using Cu_2Se-based materials

Material								
P type	N type	No. of pairs	TEG	ΔT (K)	Power density	Power output	η (%)	Ref.
Cu_2Se	Ag–Mo electrode	10	Thin film	50	4.28 W m^{-2}	70 nW	[a]	34
PEDOT:PSS coated Cu_2Se	PEDOT/Ag_2Se/CuAgSe	5	Thin film	44	4.4 W m^{-2}	1548 nW	[a]	46
70%-Sb_2Se_3/30%-β-Cu_2Se/PANI	Cu electrode	5	Thin film	30	[a]	80.1 nW	[a]	47
Cu_2Se	Ag electrode	10	Thin film	38	580.70 mW m^{-2}	3.31 nW	[a]	48
Cu_2Se	Ag_2Se	6	Thin film	40	13.4 W m^{-2}	600 nW	[a]	49
Cu_2Se-cuboid	[a]	1	Bulk	169	50 mW cm^{-2}	2500 nW	[a]	50
$Cu_2Se_{0.96}I_{0.02}Te_{0.02}$/$Cu_2O$	$InSb_{0.94}Bi_{0.06}$	6	Bulk	120	35.1 μW cm^{-2}	10.6 μW	1.74	17
$Cu_2Se_{0.94}S_{0.02}Te_{0.02}$	$Cu_{0.7}Ni_{0.3}$	8	Bulk	120	37.7 μW cm^{-2}	21.86 μW	2.07	This work

[a] Not given.

40, 60, 80, 100, and 120 K, respectively. Fig. 9f depicts P_{max} as a function of ΔT, and the power density is calculated by dividing the total output power by the cross-sectional area (2.691 mm × 2.693 mm × 8) of the TEG.[42] The maximum power density achieved is 37.7 μW cm^{-2} at $\Delta T = 120$ K.

The device figure of merit (zT_{device}) for the as-fabricated TEG is calculated using eqn (9)

$$zT_{device} = \frac{(S_p - S_n)^2 T}{\left[\sqrt{\rho_p k_p} + \sqrt{\rho_n k_n}\right]^2},\qquad(9)$$

where S_p and S_n are the Seebeck coefficients for the p-type and n-type materials, respectively; ρ and κ denote electrical resistivity and thermal conductivity, respectively.[43] Fig. 10a illustrates the temperature-dependent zT for the p-leg, n-leg, and the overall device, which increase from 0.1 at 325 K to 0.44 at 550 K.

The thermoelectric conversion efficiency (η) of the material is described by

$$\eta = \frac{T_H - T_C}{T_H}\frac{\sqrt{1+zT}-1}{\sqrt{1+zT}+\frac{T_C}{T_H}},\qquad(10)$$

where T_H is the hot side temperature and T_C the cold side temperature.[44,45] Fig. 10b shows the ideal efficiency (η) of the p-leg, n-leg, and the as-fabricated TEG. The calculations assume a fixed cold side temperature of 293 K while varying the hot side temperature from 300 K to 413 K, corresponding to temperature differences (ΔT) of 7, 20, 30, 40, 60, 80, 100, and 120 K. The maximum efficiency achieved for the p-leg, n-leg, and the TEG are 2.0%, 2.25%, and 2.07%, respectively, at $\Delta T = 120$ K and $T_H = 413$ K. Table 3 compares the performance of the fabricated TEG with results from recent studies, highlighting its competitive efficiency and figure of merit.

6. Conclusion

The synthesized series of Cu_2Se, $Cu_2Se_{0.96-x}S_xTe_{0.04}$ ($x = 0.00$, 0.01, 0.02, 0.03), and $Cu_{2-y}Se_{0.94}S_{0.02}Te_{0.04}$ ($y = 0.00$, 0.02, 0.04) demonstrates promising thermoelectric properties, with notable enhancements in electrical and thermal transport characteristics. Sulfur doping in $Cu_2Se_{0.96-x}S_xTe_{0.04}$ effectively reduces thermal conductivity and improves electrical resistivity, leading to a power factor of 10.16 μW cm^{-1} K^{-2} and a peak zT value of 1.56 at 915 K. The composition with $x = 0.02$ achieves the highest average zT (zT_{avg}) of 1.34 over the temperature range

of 750–915 K, showcasing significant thermoelectric performance enhancement.

In the $Cu_{2-y}Se_{0.94}S_{0.02}Te_{0.04}$ series, increasing copper deficiency enhances hole concentration and reduces electrical resistivity. Among these, $Cu_{1.96}Se_{0.94}S_{0.02}Te_{0.04}$ achieves the highest power factor of 10.64 μW cm^{-1} K^{-2}, a 5% improvement over $Cu_2Se_{0.94}S_{0.02}Te_{0.04}$ without copper deficiency. Weighted mobility analysis reveals a $T^{-3/2}$ dependence in the β-phase, indicating acoustic phonon scattering as the dominant electron scattering mechanism. Thermal transport analysis shows that copper-deficient samples ($y = 0.02$ and 0.04) exhibit higher thermal conductivity, which reduces zT despite improved power factors. A thermoelectric generator (TEG) comprising eight pairs of p-leg $Cu_2Se_{0.94}S_{0.02}Te_{0.04}$ and n-leg $Cu_{0.7}Ni_{0.3}$ demonstrates practical viability. The TEG achieves a maximum output voltage of 0.127 V and a peak output power of 21.86 μW at a temperature difference (ΔT) of 120 K. Conversion efficiencies of the p-leg, n-leg, and TEG device are 2.0%, 2.25%, and 2.07%, respectively, at $\Delta T = 120$ K. These findings underscore the potential of the synthesized materials for practical thermoelectric applications.

Data availability

The data supporting the findings of this study are available from the corresponding author upon reasonable request.

Conflicts of interest

There are no conflicts to declare.

Note added after first publication

This article replaces the version published on 27th January 2025, which contained an error in eqn (3). The Royal Society of Chemistry apologises for any confusion.

Acknowledgements

References

1 Z. Zhang, K. Zhao, T.-R. Wei, P. Qiu, L. Chen and X. Shi, *Energy Environ. Sci.*, 2020, **13**, 3307–3329.

2 I. Paulraj, T.-F. Liang, T.-S. Yang, C.-H. Wang, J.-L. Chen, Y.-W. Wang and C.-J. Liu, *ACS Appl. Energy Mater.*, 2020, **3**, 12447–12459.

3 H. Liu, X. Yuan, P. Lu, X. Shi, F. Xu, Y. He, Y. Tang, S. Bai, W. Zhang and L. Chen, *Adv. Mater.*, 2013, **25**(45), 6607–6612.

4 D. Sidharth, I. Paulraj, V. Lourdhusamy, M. Arivanandhan and C.-J. Liu, *J. Eur. Ceram. Soc.*, 2024, **44**, 954–960.

5 I. Paulraj, V. Lourdhusamy and C.-J. Liu, in *Handbook of Energy Materials*, Springer, 2023, pp. 1–34.

6 Z. Zhou, Y. Huang, B. Wei, Y. Yang, D. Yu, Y. Zheng, D. He, W. Zhang, M. Zou and J.-L. Lan, *Nat. Commun.*, 2023, **14**, 2410.

7 R. Nunna, P. Qiu, M. Yin, H. Chen, R. Hanus, Q. Song, T. Zhang, M.-Y. Chou, M. T. Agne and J. He, *Energy Environ. Sci.*, 2017, **10**, 1928–1935.

8 T. Day, F. Drymiotis, T. Zhang, D. Rhodes, X. Shi, L. Chen and G. J. Snyder, *J. Mater. Chem. C*, 2013, **1**, 7568–7573.

9 D. Sidharth, A. A. Nedunchezhian, R. Akilan, A. Srivastava, B. Srinivasan, P. Immanuel, R. Rajkumar, N. Y. Devi, M. Arivanandhan, C.-J. Liu, G. Anbalagan, R. Shankar and R. Jayavel, *Sustainable Energy Fuels*, 2021, **5**, 1734–1746.

10 K. Zhao, M. Guan, P. Qiu, A. B. Blichfeld, E. Eikeland, C. Zhu, D. Ren, F. Xu, B. B. Iversen and X. Shi, *J. Mater. Chem. A*, 2018, **6**, 6977–6986.

11 F. H. Lin and C. J. Liu, *ChemSusChem*, 2021, **14**, 1316–1323.

12 L. Yang, Z.-G. Chen, G. Han, M. Hong, L. Huang and J. Zou, *J. Mater. Chem. A*, 2016, **4**, 9213–9219.

13 F. Jia, S. Zhang, X. Zhang, X. Peng, H. Zhang and Y. Xiang, *Chem.–Eur. J.*, 2014, **20**, 15941–15946.

14 D. Li, X. Y. Qin, Y. F. Liu, C. J. Song, L. Wang, J. Zhang, H. X. Xin, G. L. Guo, T. H. Zou and G. L. Sun, *RSC Adv.*, 2014, **4**, 8638–8644.

15 L. Xue, C. Fang, W. Shen, M. Shen, W. Ji, Y. Zhang, Z. Zhang and X. Jia, *Mod. Phys. Lett. B*, 2020, **34**, 2050006.

16 K. Zhao, A. B. Blichfeld, H. Chen, Q. Song, T. Zhang, C. Zhu, D. Ren, R. Hanus, P. Qiu and B. B. Iversen, *Chem. Mater.*, 2017, **29**, 6367–6377.

17 V. Lourdhusamy, I. Paulraj and C.-J. Liu, *Inorg. Chem.*, 2024, **63**, 3735–3748.

18 Y.-X. Zhang, Y.-Q. Tang, Z. Ma, M.-Y. Hu, J. Feng and Z.-H. Ge, *Inorg. Chem.*, 2021, **60**, 13269–13277.

19 J. Zhang, L. Song, A. Mamakhel, M. R. V. Jørgensen and B. B. Iversen, *Chem. Mater.*, 2017, **29**, 5371–5383.

20 S. V. Faleev and F. Léonard, *Phys. Rev. B: Condens. Matter*, 2008, **77**, 214304.

21 I. Paulraj, V. Lourdhusamy, Z.-R. Yang, C.-H. Wang and C.-J. Liu, *J. Power Sources*, 2023, **572**, 233096.

22 C.-A. Wu, K.-C. Chang, F.-H. Lin, Z.-R. Yang, A. Gharleghi, T.-Z. Wei and C.-J. Liu, *Chem. Eng. J.*, 2019, **368**, 409–416.

23 N. F. Mott and E. A. Davis, *Electronic Processes in Non-crystalline Materials*, OUP Oxford, 2012.

24 V. P. Kannan, I. Paulraj, V. Lourdhusamy, C.-J. Liu and S. Madanagurusamy, *Mater. Today: Proc.*, 2022, **49**, 2761–2764.

25 V. P. Kannan, V. Lourdhusamy, I. Paulraj, C.-J. Liu and S. Madanagurusamy, *ACS Appl. Mater. Interfaces*, 2023, **15**, 47058–47069.

26 J.-D. Musah, A. Ilyas, S. Venkatesh, S. Mensah, S. Kwofie, V. A. Roy and C.-M. L. Wu, *Nano Res. Energy*, 2022, **1**, e9120034.

27 K.-C. Chang and C.-J. Liu, *Comput. Phys. Commun.*, 2020, **247**, 106875.

28 K. Zhao, A. B. Blichfeld, E. Eikeland, P. Qiu, D. Ren, B. B. Iversen, X. Shi and L. Chen, *J. Mater. Chem. A*, 2017, **5**, 18148–18156.

6040 | *J. Mater. Chem. A*, 2025, **13**, 6027–6041

This journal is © The Royal Society of Chemistry 2025

29 V. P. Kannan, V. Lourdhusamy, I. Paulraj, S. Madanagurusamy and C.-J. Liu, *ACS Appl. Mater. Interfaces*, 2024, **16**, 58677–58688.

30 V. Lourdhusamy, J.-L. Chen, I. Paulraj, L.-C. Hsu, Y.-Y. Li, T.-S. Yang, K. V. Prabu and C.-J. Liu, *J. Alloys Compd.*, 2022, **920**, 165949.

31 H.-S. Kim, Z. M. Gibbs, Y. Tang, H. Wang and G. J. Snyder, *APL Mater.*, 2015, **3**, 041506.

32 Z. Du, J. He, X. Chen, M. Yan, J. Zhu and Y. Liu, *Intermetallics*, 2019, **112**, 106528.

33 S. Choo, F. Ejaz, H. Ju, F. Kim, J. Lee, S. E. Yang, G. Kim, H. Kim, S. Jo and S. Baek, *Nat. Commun.*, 2021, **12**, 3550.

34 Z.-H. Zheng, D.-L. Zhang, B. Jabar, T.-B. Chen, M. Nisar, Y.-F. Chen, F. Li, S. Chen, G.-X. Liang and X.-H. Zhang, *Mater. Today Phys.*, 2022, **24**, 100659.

35 T. W. Day, K. S. Weldert, W. G. Zeier, B.-R. Chen, S. L. Moffitt, U. Weis, K. P. Jochum, M. Panthöfer, M. J. Bedzyk and G. J. Snyder, *Chem. Mater.*, 2015, **27**, 7018–7027.

36 H. Liu, X. Shi, F. Xu, L. Zhang, W. Zhang, L. Chen, Q. Li, C. Uher, T. Day and G. J. Snyder, *Nat. Mater.*, 2012, **11**, 422–425.

37 F. Liu, M. Huang, Z. Gong, W. Ao, Y. Li and J. Li, *J. Alloys Compd.*, 2015, **651**, 648–654.

38 S. D. Kang, J.-H. Pöhls, U. Aydemir, P. Qiu, C. C. Stoumpos, R. Hanus, M. A. White, X. Shi, L. Chen and M. G. Kanatzidis, *Mater. Today Phys.*, 2017, **1**, 7–13.

39 D. B. S. Sethuraman and C.-J. Liu, *J. Alloys Compd.*, 2024, **1010**, 177569.

40 Y.-S. Cheng, D. B. S. Sethuraman and C.-J. Liu, *J. Alloys Compd.*, 2024, **971**, 172748.

41 I. Paulraj, V. Lourdhusamy and C.-J. Liu, *Mater. Sci. Semicond. Process.*, 2025, **188**, 109252.

42 I. Paulraj, T.-F. Liang, T.-S. Yang, C.-H. Wang, J.-L. Chen, Y. W. Wang and C.-J. Liu, *ACS Appl. Mater. Interfaces*, 2021, **13**, 42977–42990.

43 I. Paulraj, V. Lourdhusamy and C.-J. Liu, *Chem. Eng. J.*, 2022, **446**, 137083.

44 V. Karthikeyan, J. U. Surjadi, J. C. Wong, V. Kannan, K.-H. Lam, X. Chen, Y. Lu and V. A. Roy, *J. Power Sources*, 2020, **455**, 227983.

45 K. V. Prabu, V. Lourdhusamy, I. Paulraj, M. Sridharan and C.-J. Liu, *Mater. Chem. Phys.*, 2023, **297**, 127379.

46 Y. Lu, X. Li, K. Cai, M. Gao, W. Zhao, J. He and P. Wei, *ACS Appl. Mater. Interfaces*, 2021, **13**, 631–638.

47 M. Kim, D. Park and J. Kim, *Polymers*, 2021, **13**, 1518.

48 X. L. Huang, D. W. Ao, T. B. Chen, Y. X. Chen, F. Li, S. Chen, G. X. Liang, X. H. Zhang, Z. H. Zheng and P. Fan, *Mater. Today Energy*, 2021, **21**, 100743.

49 J. Xie, M. Han, X. Zeng, D. Mao, H. Li, X. Zeng, R. Liu, L. Ren, R. Sun and J. Xu, *Chem. Eng. J.*, 2022, **435**, 135172.

50 S. Choo, F. Ejaz, H. Ju, F. Kim, J. Lee, S. E. Yang, G. Kim, H. Kim, S. Jo, S. Baek, S. Cho, K. Kim, J. Y. Kim, S. Ahn, H. G. Chae, B. Kwon and J. S. Son, *Nat. Commun.*, 2021, **12**, 3550.

This journal is © The Royal Society of Chemistry 2025

J. Mater. Chem. A, 2025, **13**, 6027–6041 | **6041**